Indian Journal of Pure & Applied Physics
Vol. 63, October 2025, pp. 901-909
DOI: 10.56042/ijpap.v63i10.17880

Structural, Dielectric and Magnetic Characterization of Double Perovskite $BaLaCuSbO_6$

Vibha[a*], Sujata Sanghi[a], Ashish Agarwal[a], Ekta Arya[a], Shalu Kaushik[a] & Meenal Chauhan[b]

[a]Department of Physics, Guru Jambheshwar University of Science & Technology, Hisar, Haryana 125 001, India

[b]Department of Physics, Shri Khushal Das University, Hanumangarh, Rajasthan 335 801, India

Received: 12th March 2025; accepted: 17th July 2025

This work highlights a comprehensive investigation of the structural, dielectric and magnetic properties of the double perovskite $BaLaCuSbO_6$. The material was synthesized via the solid-state reaction technique. X-Ray diffraction (XRD) and Rietveld refinement analysis confirmed that the material adopts a monoclinic structure with the I2/m space group at room temperature. The crystallite size, calculated using both the Debye-Scherrer equation and the Williamson-Hall plot, revealed nanoscale dimensions. Electron density mapping and SEM analysis confirmed structural integrity and uniform grain distribution. Dielectric studies performed over the frequency range of 10 Hz to 10 MHz exhibited strong dispersion at low frequencies, stabilizing at higher frequencies, consistent with Maxwell-Wagner polarization. Both impedance and conductivity analysis demonstrated that the material exhibits negative temperature coefficient of resistance (NTCR) characteristics, confirming its semiconducting nature at high temperatures. Modulus spectroscopy confirmed a non-Debye relaxation mechanism, and AC conductivity analysis suggested thermally activated charge transport. Magnetic characterization revealed the anti-ferromagnetic behavior of the material at room temperature, as observed from the nature of magnetic hysteresis loop. These findings suggest that $BaLaCuSbO_6$ is a promising candidate for applications in electronic and magnetic devices.

Keywords: Double perovskite oxide, Solid-State reaction technique, Nyquist plot, Semiconducting nature, Anti-ferromagnetic property

1 Introduction

Perovskite materials, defined by the general formula ABX_3, have been extensively studied due to their remarkable structural versatility and wide-ranging physical properties[1,2]. Their ability to accommodate diverse atomic substitutions enables the fine-tuning of electronic, optical, and magnetic characteristics, making them highly relevant for applications in catalysis[3], energy storage[4], spintronics[5], and optoelectronics[6]. A specialized subclass of these materials, known as ordered double perovskites, follows the structural formula $A_2B'B''O_6$ or $A'A''B'B''O_6$, where two distinct metal cations occupy the B-site in an alternating fashion[7]. This ordered arrangement significantly impacts their structural stability and functional behavior, including dielectric, magnetic, and transport properties[8,9]. The incorporation of transition metal ions at the B-site further enhances these effects by introducing strong electron-lattice interactions, resulting in emergent properties such as magneto resistance[10], multiferroicity[11], and half-metallicity[12].

Several double perovskites have been widely investigated for their potential technological applications. For instance, La_2NiMnO_6 exhibits giant magneto dielectric effects, semiconducting behavior and colossal magnetoresistance, making it a promising material for magneto electronic devices[13,14]. Sr_2FeMoO_6 has been identified as a half-metallic ferrimagnet[15] while Sr_2FeWO_6 demonstrates antiferro magnetic insulating behavior[16]. Double perovskites have found applications in photocatalysis[17], solid oxide fuel cells[18], spintronic devices[19] and memory devices[20] due to their tunable electronic and magnetic properties. However, the dielectric behavior of double perovskites is highly influenced not only by the choice of transition metal cations but also by external factors such as grain size, grain boundaries, interfacial polarization, and Maxwell-Wagner effects, necessitating further investigation into new compositions.

Motivated by the significance of double perovskites, we have synthesized and studied $BaLaCuSbO_6$, aBa^{2+}- based antimonate compound featuring Cu^{2+}at the B-site. While antimonite

*Corresponding author: E-mail: vibha600@gmail.com

perovskites have been explored for their diverse electronic behaviors, including insulating, metallic, and spin-polarized states[21-24], compositions containing Cu^{2+} remain underexplored. The objective of this study is to provide a comprehensive analysis of the structural properties, dielectric response and magnetic features of $BaLaCuSbO_6$. While the material has previously been reported by Blanco *et al.*[25], its dielectric characteristics remain unexplored. This work offers, to our knowledge, the first detailed evaluation of $BaLaCuSbO_6$, presenting novel perspectives on its structure-property correlations.

2 Experimental Details

The synthesis of $BaLaCuSbO_6$ double perovskite was carried out using a solid-state reaction approach. High-purity analytical-grade reagents (purity >99.0%) were employed, including $BaCO_3$, La_2O_3, CuO and Sb_2O_3. The raw materials were precisely weighed in stoichiometric proportions, followed by grinding for 12 h in the presence of acetone as a volatile medium to ensure homogeneity. The resulting mixture underwent sequential thermal treatments: pre-heating at 750°C and 850°C for 20 h each, and final sintering at 1150°C for 20 h. Intermediate grinding for 30 minutes was performed between each heat treatment, with all thermal treatments executed at a controlled heating rate of 3°Cmin^{-1}.

Structural characterization was carried out via X-Ray Diffraction (XRD) at room temperature with a Rigaku Miniflex II diffractometer, using Cu Kα radiation (scanning range: 10°-80°, scanning rate: 2°min^{-1}, step size: 0.02°). Structural refinement and determination of lattice parameters were conducted using Full Prof software. The surface morphology of the synthesized material was analyzed through Scanning Electron Microscopy (SEM) and Energy Dispersive X-Ray (EDX) using FESEM (JEOL, JSM-7800F). For electrical characterization, compact cylindrical pellets with a diameter of 10 mm were prepared by uniaxially pressing the powder (with 3wt% PVA as binder) using a Hydraulic Pellet Press under an applied pressure of 100 torr for a duration of 90 seconds. Silver electrodes were deposited on opposite faces of the pellets and impedance spectroscopy was conducted with a Novo control Impedance Analyzer (Concept 50) across a wide frequency and temperature range. Magnetic properties were analyzed out using a Vibrating Sample Magnetometer (VSM) at room temperature.

3 Results and Discussion

3.1 Structural Studies

Figure. 1 displays the XRD pattern at room temperature, which was used to determine the phase composition of the synthesized material. A polycrystalline structure is confirmed by the diffraction pattern, with a slight impurity peak marked with a star. The crystal structure was further examined by applying Rietveld refinement to the XRD data using Full Prof software[26]. Rietveld method employs a least-squares approach to iteratively refine a theoretical diffraction profile until it closely matches the experimentally measured pattern. A preliminary structural model, representative of the true crystal structure, serves as starting point for the refinement process.

The refinement process was quantified and optimized using weighted profile parameters, such as R_p and R_{wp}, to attain convergence and maintain the goodness of fit (χ^2) near unity. The refined XRD profile reveals an excellent agreement between simulated and experimental patterns, as evidenced by the close fit. The analysis confirms that $BaLaCuSbO_6$ crystallizes in a monoclinic phase corresponding to the I2/m space group. The crystallographic

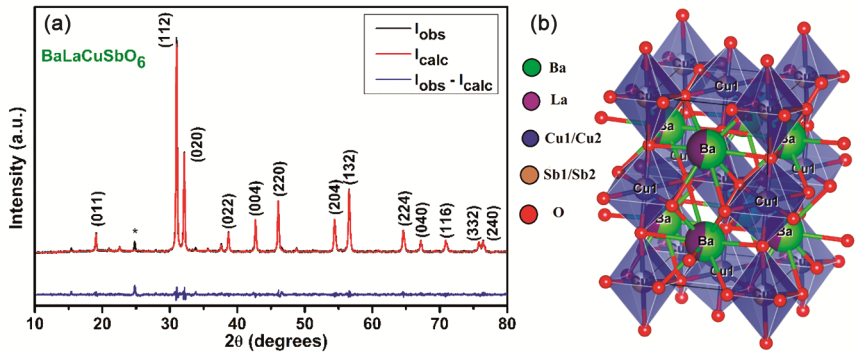

Fig. 1 — (a) Room temperature Rietveld-refined XRD pattern; and (b) Structural representation of $BaLaCuSbO_6$ by VESTA program

Table 1 — Rietveld refined structural parameters of $BaLaCuSbO_6$

Composition	$BaLaCuSbO_6$
Lattice parameters	a = 5.5713(4) Å
	b = 5.5694(4) Å
	c = 8.4663(3) Å
	V = 262.69(2) Å^3
	β = 90.111(3)°
R- factors	
R_p	6.29
R_{wp}	9.04
χ^2	3.57

Positional Coordinates

Atom	x	y	z
Ba	0.4902(7)	0.0000	0.2514(9)
La	0.4902(7)	0.0000	0.2514(9)
Cu1	0.0000	0.0000	0.5000
Cu2	0.0000	0.0000	0.0000
Sb1	0.0000	0.0000	0.5000
Sb2	0.0000	0.0000	0.0000
O1	-0.0810(3)	0.0000	0.2760(3)
O2	0.2984(19)	0.2170(3)	-0.0352(13)

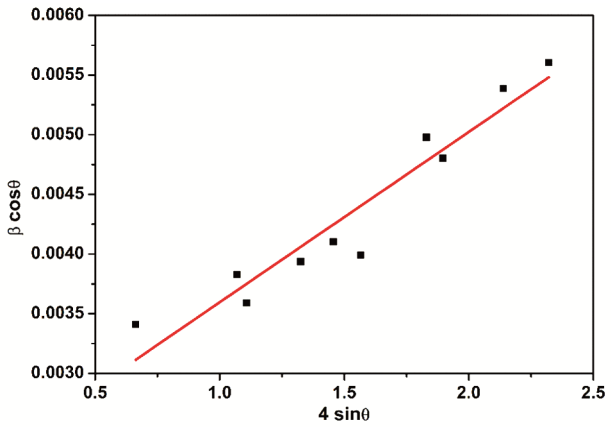

Fig. 2 — Crystallite size estimation using Williamson Hall approach

parameters, profile R-factors and atomic positional coordinates are summarized in Table 1. A schematic representation of the $BaLaCuSbO_6$ structure, visualized through the VESTA software, is shown in Fig. 2. The interatomic distances and bond angles determined via Rietveld refinement are summarized in Table 2. Analysis of the data in Table 2 reveals that the bond angles for Cu/Sb-O1-Cu/Sb and Cu/Sb-O2-Cu/Sb are less than 180°, indicating a rotational distortion of the CuO_6 and SbO_6 polyhedra, which further corroborates the monoclinic structure of the material.

The structural stability of double perovskites is associated with the tolerance factor (t), which determines the symmetry of the crystal lattice.

Table 2 — Bond lengths and Bond angles of $BaLaCuSbO_6$ derived from Rietveld refinement

Bond Distances (Å)	
Ba/La—O1 (×2)	2.840(4)
Ba/La—O2 (×2)	2.912(14)
Ba/La—O2 (×2)	2.491(14)
Ba/La—O2 (×2)	2.947(14)
Cu1/Sb1—O1 (×2)	1.950(3)
Cu1/Sb1—O2 (×2)	1.958(18)
Cu2/Sb2—O1 (×2)	2.380(3)
Cu2/Sb2—O2 (×2)	2.077(13)
Bond Angles (°)	
O1—Cu/Sb—O2	72.9(10)
O1—Cu/Sb—O2	73.7(12)
O1—Cu/Sb—O2	108(8)
Cu/Sb—O1—Cu/Sb	155.7(10)
Cu/Sb—O2—Cu/Sb	154.9(6)

Typically, an ideal cubic structure is maintained when t ranges between 1.05 and 1.00. A slight distortion leading to tetragonal symmetry occurs for t values between 1.00 and 0.97. When t falls below 0.97, the structure tends to adopt either monoclinic or orthorhombic symmetry. The tolerance factor is determined using the Golschmidt tolerance factor Eq.[27]

$$t = \frac{\frac{R_A + R_{A'}}{2} + R_0}{\sqrt{2}\left[\frac{R_B + R_{B'}}{2} + R_0\right]} \quad \ldots (1)$$

where the Shannon ionic radii of A and B-site metal ions are denoted by R_A, $R_{A'}$, R_B and $R_{B'}$ while R_O denotes the oxygen ion radius. For $BaLaCuSbO_6$, the calculated t value comes out to be0.94, confirming its deviation from cubic symmetry and supporting its monoclinic structure.

The average crystallite size for the prepared sample was calculated using Debye Scherrer formula Eq.[28]

$$D_{SC} = \frac{0{\cdot}9\lambda}{\beta \cos\theta} \quad \ldots (2)$$

Where λ stands for the X-Ray wavelength, 0.9 for the Scherrer constant, D_{SC} for the crystallite size and β stands for the full width measured at half of the diffraction peak's maximum intensity (FWHM). The crystallite size estimated using this method was found out to be 35 nm. In addition to this, the Williamson-Hall (WH) analysis provides an alternating approach to evaluate the crystallite size by considering peak broadening effects. According to the WH method, the broadening of X-Ray diffraction peaks arises from

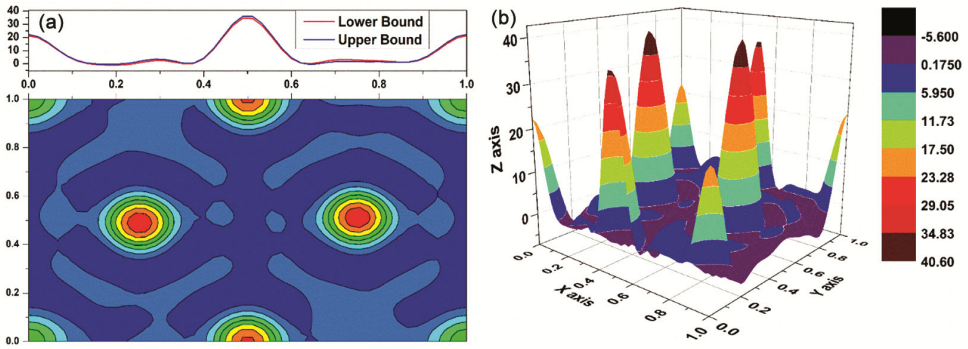

Fig. 3 — (a) 2D contour map; and (b) 3D electron density map of $BaLaCuSbO_6$

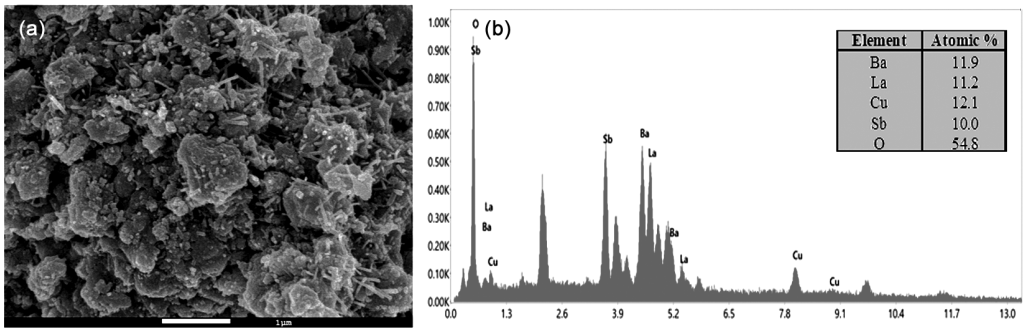

Fig. 4 — (a) SEM micrograph; and (b) EDX spectrum of $BaLaCuSbO_6$ double perovskite

both crystallite size and microstrain contributions. The total peak broadening can be expressed as[29]:
and

$$\beta\, cos\theta = \frac{0{\cdot}9\lambda}{D_{WH}} + 4\,\varepsilon\, sin\theta \qquad \ldots (3)$$

where D_{WH} represents the crystallite size obtained via the WH method and ε denotes the microstrain. The crystallite size D_{WH} was determined from the intercept of the plot shown in Fig. 2 and was found to be 66 nm, indicating a significant contribution of microstrain to the peak broadening.

To gain deeper insights into the structural variations, electron density maps were analyzed using GFourier maps. These maps facilitate the visualization of valence electron distributions through an appropriate localization framework, allowing the detection of harmonic variations induced by atomic positional shifts. The atomic structure factor corresponding to different diffraction peaks is given by[30]:

$$F_{hkl} = \iiint_{000}^{abc} \rho(x,y,z) e^{2\pi i(hk+ky+lz)} dxdydz \qquad \ldots (4)$$

The inverse Fourier transform of this equation provides the electron density distribution as:

$$\rho(x,y,z) = \frac{1}{V}\sum F_{hkl}\, e^{-2\pi i(hk+ky+lz)} \qquad \ldots (5)$$

This equation enables the estimation of electron density across different crystal structures. The 2D (x-z plane) and 3D electron density maps for the synthesized sample are illustrated in Fig. 3(a-b). The overlap of the upper and lower bounds in the 2D contour map reflects the intrinsic symmetry of the material, while the 3D electron density map indicates significantly higher electron densities for Ba/La atoms compared to Cu/Sb and O atoms, which can be attributed to their higher atomic numbers.

Fig. 4(a) displays a scanning electron microscopy (SEM) micrograph of the synthesized sample. Microstructural analysis demonstrates uniform distribution of grains of various dimensions across the sample surface, with the presence of small voids. The elevated processing temperatures contribute to increased particle growth. It is noteworthy that the crystallite size ascertained by X-Ray diffraction examination is substantially smaller than the grain size estimated from the SEM image, which falls in the micrometer range. This implies that a grain is made up of multiple crystallites, indicating a well-defined polycrystalline nature of the material. Fig. 4(b) presents the EDX results, derived from SEM analysis, confirming the presence of all the constituent elements from the initial raw materials in the

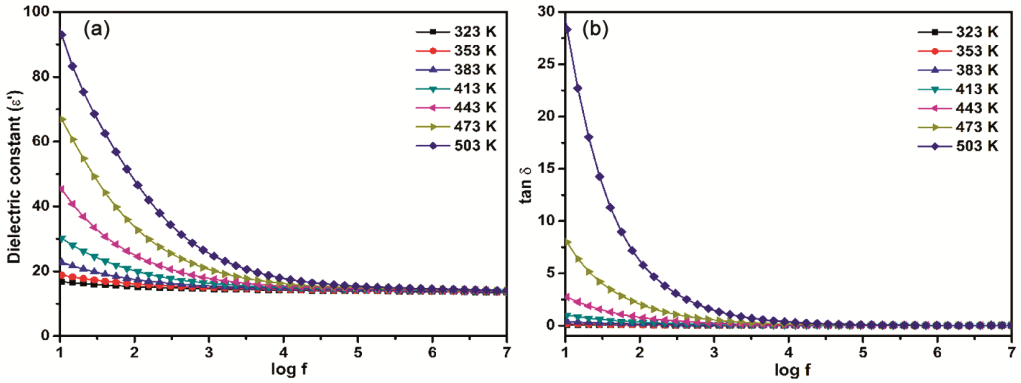

Fig. 5 — Variation of (a) Dielectric constant; and (b) Dielectric loss of $BaLaCuSbO_6$as a function of frequency

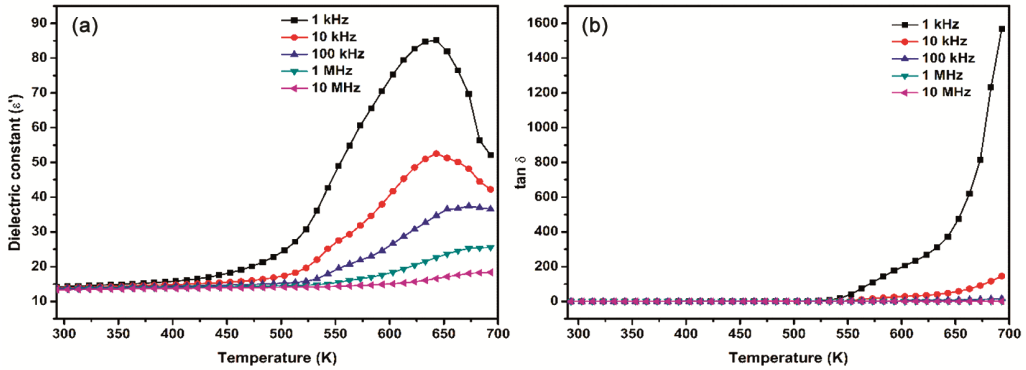

Fig. 6 — Variation of (a) Dielectric constant; and (b) Dielectric loss of $BaLaCuSbO_6$ as a function of temperature

synthesized samples and validating the elemental composition.

3.2 Dielectric Studies

The frequency-dependent behavior of the dielectric constant (ε′) and dielectric loss (tan δ) of the synthesized material in the temperature range 323 – 523 K is illustrated in Fig. 5(a) and 5(b), respectively. Both parameters exhibit significant dispersion behavior in the low-frequency region, whereas at higher frequencies, they tend to stabilize, approaching a nearly constant value. This characteristic response of the dielectric constant arises from the combined effect of dipole orientational relaxation and charge carrier conduction. A high dielectric constant in the low frequency range can be ascribed to multiple contributing factors such as charge defects, grain boundary effects, oxygen vacancies and interfacial dislocations[31]. Various polarizations, including electronic, ionic, orientational and interfacial-hinder the effective alignment of charge carriers with the applied electric field resulting in an elevated dielectric constant. Nevertheless, the contributions from all polarizations except electronic polarization diminish when the frequency rises above a certain point. Thus, the dielectric constant gradually declines as a result of this decrease in overall polarizability. This phenomenon is well explained by Maxwell-Wagner polarization model and Koop's phenom enological theory of space charge relaxation in heterogeneous systems. Koop's two-layer model describes the material as consisting of strongly conductive grains separated by grain boundaries of low conductivity. In the low frequency region, grain boundaries dominate the dielectric response, hindering the electron transport across them[32]. Consequently, charge accumulation at grain boundaries leads to space charge polarization, thereby increasing the dielectric constant. In contrast, at high frequencies, space charge polarization diminishes as electron hopping between different valence states of Fe and Ti ions fails to align with the rapidly alternating electric field, resulting in a lower dielectric constant. Furthermore, at higher frequencies, grains exhibit increased electrical conductivity, reducing dispersion effects and minimizing the dielectric losses.

Fig. 6 (a-b) illustrate the temperature-dependent variation of the dielectric constant and dielectric loss. Both parameters exhibit an increasing trend with

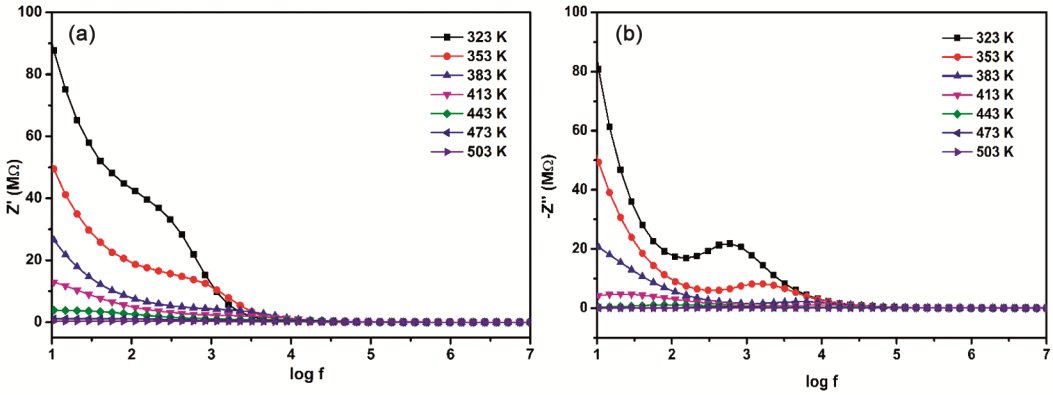

Fig. 7 — Variation of (a) real and (b) imaginary part of impedance with frequency for $BaLaCuSbO_6$

temperature. The dielectric constant initially rises gradually, reaches a broad maximum, and subsequently declines. Notably, this peak moves to higher temperatures with an increase in frequency. In contrast, dielectric loss vs temperature plot does not exhibit a distinct peak. This trend may be explained by the presence of oxygen vacancies and interfacial polarization at high temperatures. At lower temperatures, the weak polarization response results in a lower dielectric constant. On the other hand, the dielectric constant increases as temperature rises, because the thermal energy available to electric dipoles facilitates dipole orientation, enabling their alignment with the applied electric field, which results in an increase in dielectric constant.

3.3 Impedance Studies

The frequency-dependent variation of the real (Z') and imaginary (Z'') components of impedance at different temperatures is shown in Fig. 7 (a-b). The conductive nature of the material is characterized by Z' decreasing with increasing frequency and temperature, in the low-frequency region. This behavior further confirms the presence of a negative temperature coefficient of resistance (NTCR)[30], indicative of semiconducting properties. Additionally, since all of the curves converge at frequencies higher than 10^4 Hz, it suggests that the space charges are released and the barrier properties consequently diminish[34].

A temperature-dependent relaxing process is evident in Fig. 7(b), where the loss spectrum shows a prominent peak that moves towards higher frequencies as temperature rises[35]. Furthermore, the peak height of the maximum loss factor represents the resistance encountered by both the grain and grain boundary during charge carrier transport within the material. Grain and grain boundary resistance decreases with temperature, as evidenced by the observed drop in peak height with temperature. The relaxation time (τ) is determined using the relation $\omega\tau = 1$, where ω denotes the relaxation frequency. Furthermore, the observed asymmetric broadening of the peak points to a distribution of relaxation times, implying that multiple electrical processes are involved within the material[30].

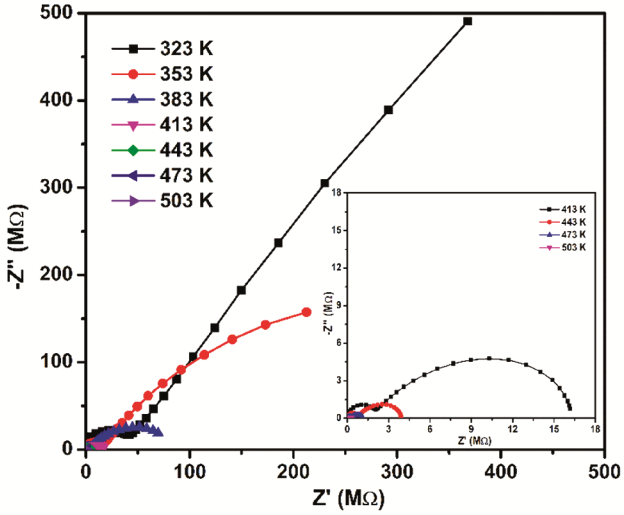

Fig. 8 — The Complex plane (Nyquist) plot of $BaLaCuSbO_6$ double perovskite

To establish a connection between the electrical and micro structural characteristics of the prepared compound, the Nyquist (complex impedance plane) plot was analyzed across a broad frequency range and temperature range of 323 K – 503 K, as depicted in Fig. 8. The combined impact of grain and grain boundary effects on the relaxation processes is reflected in the semicircular arcs seen in the impedance spectra. The presence of depressed semicircles, whose centers lie below the real

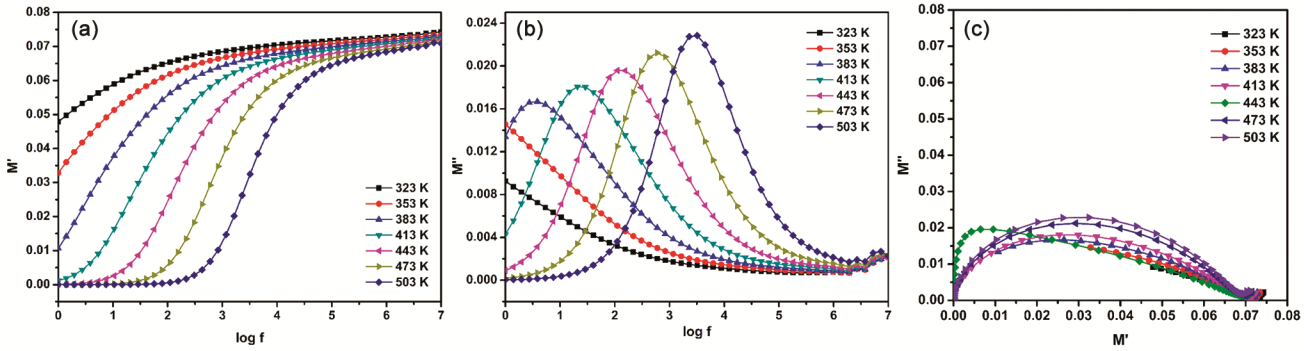

Fig. 9 — Variation of (a) the real part (b) the imaginary part of modulus with frequency(c) the complex electric modulus of BaLaCuSbO$_6$

impedance axis, suggests a departure from ideal Debye behavior. Additionally, at 323 K, the low frequency region of the plot displays a characteristic linear spike, which can be attributed to the interfacial polarization at lower temperatures. A similar effect has been previously reported by Dhiman *et al*[36]. The observed decrease in the real part of impedance (Z') with increasing temperature and frequency suggests a reduction in bulk resistance, leading to enhanced electrical conductivity. This behavior is characteristic of semiconducting nature of a material and confirms the negative temperature coefficient of resistance (NTCR) effect, wherein conductivity improves with increasing temperature.

3.4 Modulus Studies

Modulus spectra are commonly employed alongside impedance spectra to differentiate between the contributions from microscopic processes governing long-range translational motion, which influences the dynamics of charge carriers. To analyze the effects of electrode polarization, bulk properties, grain boundary conduction, electrical conductivity and relaxation behavior in the material, the electric modulus formalism has been applied. Fig. 9 (a) presents the variation of real part of modulus (M') as a function of frequency at various temperatures for the prepared double perovskite. At lower frequencies, M' approaches zero, indicating negligible electrode polarization. The absence of a restoring force for charge flow under a static electric field is reflected in the gradual rise of M' with increasing frequency, which suggests the occurrence of conduction processes and limited charge carrier mobility over short distances[37], highlighting the absence of restoring force for charge flow under a static electric field. At higher frequencies, the nearly constant M' value across different temperatures may be attributed to the suppression of space charge polarization.

Fig. 9 (b) illustrates the temperature-dependent frequency variation of the imaginary component of modulus (M'') for BaLaCuSbO$_6$. The appearance of a peak in the M'' spectrum signifies a relaxation process. The observed shift of the relaxation peak towards lower frequencies on cooling the material suggests a reduction in the relaxation rate with decreasing temperature. The frequency range below the peak maximum is associated with long-range mobility of charge carriers. In contrast, the movement of charge carriers is limited to shorter distances at frequencies higher than the peak, because they get trapped inside the localized potential wells[38]. Additionally, the peak broadening and asymmetry indicate the existence of a non-Debye relaxation process characterized by a distribution of multiple time constants.

Fig. 9 (c) depicts the complex modulus plot, showing a prominent semicircle with an indication of a second semicircle, which points to the existence of two distinct relaxation processes. Furthermore, the observed depressed semicircular arcs indicate a departure from the ideal Debye type relaxation model. This feature supports the semiconducting behavior and suggests a thermally driven conduction mechanism[39].

3.5 Conductivity Studies

Fig. 10 illustrates the temperature-dependent frequency response of the AC conductivity of BaLaCuSbO$_6$ double perovskite. The conductivity spectra exhibit two distinct regions: a plateau at lower frequencies and a dispersive region at higher frequencies. The plateau region extends to higher frequencies as temperature increases and is primarily associated with DC conductivity. In the low-

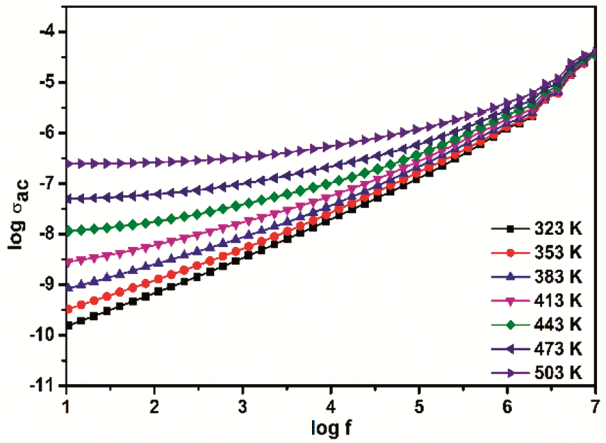

Fig. 10 — Plot of AC conductivity of $BaLaCuSbO_6$ double perovskite

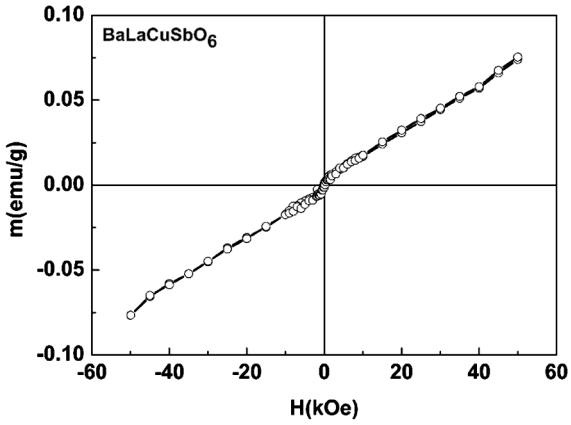

Fig. 11 — Room temperature M-H loop of $BaLaCuSbO_6$ double perovskite

frequency regime, the frequency independent conductivity can be attributed to the random diffusion of charger carriers. At higher temperatures, the hopping of charge carriers to adjacent unoccupied lattice sites facilitates long-range translational motion, which contributes to DC conductivity in this region[40]. In contrast, at higher frequencies, the conductivity exhibits a dispersive behavior due to a mismatch between carrier charge hopping and relaxation processes. The frequency at which peak appears indicates the transition in charge carrier mobility. It can be clearly noticed that this peak shifts to higher frequencies with rise in temperature. This shift can be attributed to the enhanced thermal energy acquired by charge carriers at elevated temperatures, thereby increasing their mobility.

3.6 Magnetic Studies

Fig. 11 presents the room-temperature magnetization curve of $BaLaCuSbO_6$ measured under an applied magnetic field ranging from -60 to +60 kOe. The magnetization response exhibits a nearly linear trend with no significant hysteresis loop, indicating the absence of ferromagnetic ordering. Furthermore, the magnetization does not reach saturation even under a high applied field of 60 kOe, suggesting a dominant antiferromagnetic nature. The observed low magnetic moment can be attributed to antiferromagnetic (AFM) interactions within the material[41]. This behavior is consistent with prior studies on Y_2CoMnO_6 conducted by Das *et al.*[42], where similar AFM interactions were reported. The antiferromagnetic coupling in $BaLaCuSbO_6$ can be ascribed to Cu^{2+}—O—Cu^{2+} and Sb^{5+}—O—Sb^{5+} exchange interactions. Additionally, previous magnetic investigations by Blanco *et al.* employed analytical functions to describe the diverse magnetic interactions present in the sample, further corroborating the AFM nature of the sample.

4 Conclusion

The present work shows that the double perovskite $BaLaCuSbO_6$ crystallizes in a monoclinic phase with structural stability confirmed by tolerance factor calculations and bond angle analysis. Dielectric measurements conducted over the frequency range of 10 Hz to 10 MHz revealed a high dielectric constant (~ 95) at 503 K in the low-frequency region, primarily attributed to space charge polarization effects. The semiconducting nature of the material is supported by impedance analysis, which confirms a negative temperature coefficient of resistance (NTCR). The Nyquist plot demonstrates the influence of grain and grain boundary effects on the relaxation process. Modulus spectroscopy analysis reveals a relaxation behavior characteristic of the non-Debye type. AC conductivity confirms thermally activated charge carrier transport. Magnetic measurements at room temperature indicate antiferromagnetic ordering due to Cu^{2+}—O—Cu^{2+} and Sb^{5+}—O—Sb^{5+} interactions.

Due to its significant semiconducting nature and antiferromagnetic behavior, $BaLaCuSbO_6$ holds strong potential for multifunctional applications particularly in capacitor-based energy storage systems and magneto electric or spintronic devices. Further studies could focus on doping or elemental substitution to tune its electrical and magnetic responses, enabling optimization for specific applications. Investigations into temperature-dependent magnetic ordering and magneto-dielectric coupling effects would further

expand its utility in multifunctional device engineering. Additionally, first-principle calculations could offer insights into the electronic structure and support the experimental observations.

References

1 Vasala S & Karppinen, *Prog Solid State Ch*, 43 (2015) 1.
2 Tejuca L G & Fierro J L G, *CRC Press* (1992) DOI: 10.1201/9781482277258.
3 Hou X, Ren J, Li F, Ma C, Zhang X & Feng H, *IOP Conf Ser Earth Environ Sci*, 295 (2019) 032020.
4 Han B, Zhao J, Luo Z, Cai F, Yuan Z, Zeng H, *Nano Energy*, 115 (2023) 108646.
5 Xu J, Li K, Huynh U N, Fadel M, Huang J, Sundararaman R, Vardeny V & Ping Y, *Nat Commun,* 15 (2024) 1.
6 Liu X, Wang Y, Wang Y, Zhao Y, Yu J, Shan X, Tong Y, Lian X, Wan X, Wang L, Tian P & Kuo H C, *Nanotechnol Rev*, 11 (2022) 3063.
7 Iwakura H, Einaga H & Teraoka Y, *J Novel Carbon Resour Sci,* 3 (2011) 1.
8 Baran E J, *Catalysis Today*, 8 (1990) 133.
9 Meneghini C, *Phys Rev Lett*, 103 (2009) 046403.
10 Ding L, Khalyavin D D, Manuel P, Blake J, Orlandi F, Yi W & Belik A A, *Acta Mater*, 173 (2019) 20.
11 Gaikwad V M, Dash B B, Lad A B, Chaudhari P R, Pahune B S, Shirbhate S C & Acharya S A, *Mater Chem Phys*, 275 (2022) 125326.
12 Tang Q & Zhu X, *J Mater Chem C*, 41 (2022) 15301.
13 Dass R I, Yan J Q & Good enough J B, *Phys Rev B*, 68 (2003) 064415.
14 Rogado N S, Li J, Sleight A W & Subramanian M A, *Adv Mater*, 17 (2005) 2225.
15 Kobayashi K I, Kimura T, Sawada H, Terakura K & Tokura Y, *Nature*, 395 (1998) 677.
16 Kawanaka H, Hase I, Toyama S & Nishihara Y, *J Phys Soc Jpn*, 68 (1999) 2890.
17 Amoli M R, Abedini E, Alizadeh A & Shariatinia Z, *J Ind Eng Chem*, 129 (2024) 579.
18 Huang Y H, Dass R I, Xing Z L & Good enough J B, *Science*, 312 (2006) 254.
19 Irfan M, Murtaza G, Muhammad N, Tahir S, Raza H H, Sabir B, Iftikhar M & Sharif S, *Physica E Low Dimens Syst Nanostruct*, 148 (2023) 115635.
20 Muscarella L A &Hutter E M, *ACS Energy Lett*, 7 (2022) 2128.
21 Jose R, Konopka J, Yang X, Konopka A, Ishikawa M & Koshy J, *Mod Phys Lett B,* 11 (1997) 889.
22 Kavitha V T, Jose R, Wariar P R S, Ramkrishna S & Koshy J, *Bull Mater Sci*, 34 (2011) 661.
23 Saines P J, Kennedy B J, Elcombe, Harris H H, Jang L Y & Zhang Z, *Solid State Chem,* 181 (2008) 2941.
24 Fu W T & Ijdo D J W, *J Solid State Chem*, 178 (2005) 2363.
25 Blanco M C, Paz S A, Nassif V M, Guimpel J J & Carbonio R E, *Dalton Trans,* 44 (2015) 10860.
26 Carvajal R, *J Physica B*, 192 (1993) 55.
27 Amritha krishnan B & Subodh G, *Mater Res Bull,* 93 (2017) 177.
28 Triana C A, Tellez D L, Rodriguez J A, Fajardo F & Roa-Rojas J, *Mater Lett,* 82 (2012) 116.
29 Islam S A & Ikram M, *Rare Metals,* 38 (2019) 805.
30 Vibha, Chauhan M, Arya E, Kumari A, Sanghi S & Agarwal A, *J Mater Sci Mater Electron,* 35 (2024) 1.
31 Parida K, Dehury S K & Choudhary R N P, *Phys Lett A,* 380 (2017) 4083.
32 Kumar D S, Naidu K C B, Rafi M M, Nazeer K P, Begam A A & Kumar g R, *Mater Sci Pol,* 36(2018) 123.
33 Barick B K, Mishra K K, Arora A K, Choudhary R N P & Pradhan D K, *J Phys D ApplPhys,* 44 (2011) 355402.
34 Ganguli M, Bhat M H & Rao K J, *Phys Chem Glasses,* 40 (1999) 297.
35 Alvarez F & Alegria A, *J Phys Rev B,* 56 (1997) 11377.
36 Dhiman S, Meena R, Manyani N & Tripathi S K, *Surf Interfaces,* 42 (2023) 103362.
37 Das R, Alagarsamy P & Choudhary RNP, *Phys Status Solidi B Basic Res,* 258 (2021) 2100219.
38 Bharti C, Dutta A & Sinha T P, *Solid State Sci,* 14 (2012) 920.
39 Vinnik, Zherebtsov, Gudkova, Niewa, Zabeivorota & Podgornov F V, *Ceram Int,* 42 (2016) 787.
40 Maji P, Chatterjee S & Das S, *Ceram Int,* 45 (2019) 6012.
41 Vasala S, Cheng J G, Yamachi H, Goodenough J B & Karppinen M*, Chem Mater,* 24 (2012) 2764.
42 Das R & Choudhary R N P, *Ceram Int,* 47 (2021) 439.